



HAL
open science

Temperature influence on MBS latex aggregate morphology

Ali Hamieh, Carole Coufort-Saudejaud, Aline Couffin, Alain Liné, Christine Frances

► **To cite this version:**

Ali Hamieh, Carole Coufort-Saudejaud, Aline Couffin, Alain Liné, Christine Frances. Temperature influence on MBS latex aggregate morphology. *Colloids and Surfaces A: Physicochemical and Engineering Aspects*, 2023, 676, Part A, 32 p. 10.1016/j.colsurfa.2023.132139 . hal-04261200

HAL Id: hal-04261200

<https://hal.science/hal-04261200>

Submitted on 26 Oct 2023

HAL is a multi-disciplinary open access archive for the deposit and dissemination of scientific research documents, whether they are published or not. The documents may come from teaching and research institutions in France or abroad, or from public or private research centers.

L'archive ouverte pluridisciplinaire **HAL**, est destinée au dépôt et à la diffusion de documents scientifiques de niveau recherche, publiés ou non, émanant des établissements d'enseignement et de recherche français ou étrangers, des laboratoires publics ou privés.

Copyright

Author version of the paper:

Temperature influence on MBS latex aggregate morphology
Ali Hamieh, Carole Coufort-Saudejaud, Aline Couffin, Alain Liné, Christine Frances

Colloids and Surfaces A: Physicochemical and Engineering Aspects 676 (2023) 132139

<https://doi.org/10.1016/j.colsurfa.2023.132139>

Received 15 March 2023; Received in revised form 18 July 2023; Accepted 24 July 2023

Available online 25 July 2023

0927-7757/© 2023 Published by Elsevier B.V.

Temperature influence on MBS latex aggregate morphology

Ali Hamieh ^{a,b}, Carole Coufort-Saudejaud ^a, Aline Couffin ^c, Alain Liné ^b, Christine Frances ^{a*}

^aLaboratoire de Génie Chimique, Université de Toulouse, CNRS, INPT, UPS, Toulouse, France

^bToulouse Biotechnology Institute, Université de Toulouse, CNRS, INRAE, INSA, Toulouse, France

^cARKEMA FRANCE, Groupement de Recherches de Lacq, France

* Corresponding Author: Christine Frances, christine.frances@toulouse-inp.fr

Abstract

This paper aims to better understand the impact of process conditions on the morphological properties of MBS (Methacrylate Butadiene Styrene) core-shell latex aggregates during an aggregation process. Laboratory scale experiments were performed in a stirred reactor following a standard industrial procedure including a first destabilization step by adding acid at a moderate temperature followed by a second heating step. The size and shape distribution of the aggregates as well as their fractal dimension were measured by laser diffraction and image analysis. The experimental data were analyzed in terms of number and volume distributions to obtain information on the entire population, from primary nanoparticles to aggregates several orders of magnitude larger. The main new finding of this work concerns the influence of the aggregation temperature on the size, shape and structure of latex aggregates. Indeed, the closer the temperature is to the glass transition of the MBS shell polymer, the better the agglomeration and the aggregates formed tend to be larger and more circular.

Keywords : Agglomeration – Coagulation – Particle size distribution – Circularity – Fractal dimension – Glass transition temperature

1. Introduction

The synthesis of grafted copolymers in the form of particle suspensions is often achieved by emulsion polymerization. To be used as an impact modifier for improving material properties, the latex suspension is for specific applications subjected to an aggregation process to recover the product as a dry powder with specific properties: regular shape, narrow particle diameter distribution, high bulk density for storage and transportation, and low fines content for safety and environmental reasons [1]. In particular, MBS (Methacrylate Butadiene Styrene) aggregates are used as modifiers in the PVC manufacturing process to improve impact resistance and processability. Their morphological properties have an important effect on the functional properties of the final product [2-4]. They can be controlled by monitoring the physical mechanisms during the aggregation process.

In practice, the destabilization of a stable suspension of primary particles is most often achieved adding a coagulant or changing the pH of the suspension which will act on the charged surface of the particles and lead to their collision [5]. Aggregation studies of latex colloidal systems are usually performed under turbulent conditions in a stirred tank. Spicer

and al. [6] were among the firsts to investigate the influence of the shear rate and coagulant concentration on latex aggregation in a stirred tank by studying the evolution of the size and structure of polystyrene aggregates by image analysis. The study of Kuster *et al.* [7] also focused on the effects of the impeller speed and the concentration on latex aggregation kinetics, final size distribution, and structure of aggregates. Selomulya *et al.* [8] highlighted the shear rate dependence on the restructuring and breakup of latex aggregates. In their study, the evolution of the size and structure of latex particle aggregation induced by shear was observed using small angle light scattering. This influence of the shear rate has led some authors to analyze the impact of breakage and regrowth steps on the size and morphology of latex aggregates in stirred tanks under industrially relevant conditions [9-10]. Other studies have examined the performance of sequenced hydrodynamic flocculation experiments inside a Taylor-Couette reactor, as the hydrodynamics and flow regimes inside this type of reactor are well characterized and controlled [11-13]. Moreover, Ehrl *et al.* [14] investigated the effect of primary particle size on the latex aggregate size and structure for different values of shear rate and solid volume fraction. Furthermore, besides the effect of mixing, Kostansek [15] was interested in the effect of coagulation temperature on the morphology of latex aggregates. He found that the size of the aggregates increases significantly as the coagulation temperature increases above the glass transition temperature of the copolymer.

To cover most of the relevant parameters affecting more specifically the aggregation of MBS latex by charge neutralization in a stirred tank, Li *et al.* [1] investigated the effects of pH, temperature, feeding mode, agitation, polymer concentration, and residence time on the properties of the aggregates by image analysis. According to this study, to produce spherical aggregates with uniform size and high bulk density, the amount of coagulant must be strictly controlled to achieve a well-specified pH range. Moreover, larger aggregates appeared with increasing temperature: a linear correlation is found between temperature and average particle diameter. Whereas the increase in the agitation speed induces a decrease in the mean particle diameter and a narrower size distribution.

The objectives of the present work are to better understand the aggregation mechanisms of MBS latex and more specifically to analyze the effect of temperature on the morphological properties of aggregates, defined in terms of size, shape and fractal dimensions. The coupled influence of the physicochemistry of the medium and the hydrodynamics of the reactor on the morphological properties of MBS latex aggregates is investigated. For this purpose, aggregation experiments of a latex nanoparticle suspension in presence of a sulfuric acid solution were performed in a laboratory-scale stirred reactor under standard industrial conditions. During the different phases of the process, samples were collected and analyzed using a particle size analyzer and a microscope coupled to an image analysis software to analyze the change of size and shape distributions as well as fractal dimension over time. The experimental data were analyzed in terms of number, surface, and volume distributions to obtain information on the entire population, from primary particles to agglomerates several orders of magnitude larger. The mechanical properties of the material were also characterized via DMA (Dynamic Mechanical Analysis) analysis in order to highlight the relationship between the process conditions and the morphological properties of the agglomerates produced.

2. Materials and methods

2.1 Materials

The experimental study was carried out using a suspension of MBS latex nanoparticles supplied by the industrial group ARKEMA France. The mass fraction of solids in the initial suspension is 43%. The nanoparticles are made of a spherical core-shell copolymer based on polybutadiene and polymethyl methacrylate synthesized by emulsion polymerization and stabilized by the potassium salt of fatty acid (anionic surfactant) [16]. An aqueous sulfuric acid solution having an initial concentration of 1 mol/l and a density of 1.06 Kg/l from Lch Chimie was chosen as coagulant and pellets of sodium hydroxide with a purity >98% from Sigma-Aldrich were used to neutralize the pH of the suspension after destabilization.

2.2 Characterization of the MBS latex and slurries

2.2.1 Morphological properties of the particles

The morphological properties of particles refer to their properties of size, shape and fractal dimension.

Laser diffraction

The particle size distributions of the initial and agglomerated suspensions were determined by laser diffraction using a Mastersizer 3000 equipped with the liquid sample dispersion unit Hydro MV (Malvern Panalytical®). The refractive index and the absorption index of the latex are 1.528 and 0.1, respectively. The results will be presented as volume, surface or number distributions according to particle size classes. Laser diffraction allows obtaining an equivalent optical spherical diameter. The number and surface distributions were then deduced from the volumetric distribution by calculating the number and surface corresponding to the volumetric fraction for each size class. From these distributions, the values of characteristic diameters can be obtained, among which the mode, which refers to the most probable size, and the median diameter, which is widely used in particulate processes and refers to the value where half of the population resides above this point, and half resides below this point.

The volume, surface, and number distributions of the initial MBS latex suspension are shown on the same graph in Figure 1. The median diameters are 410, 380, and 340 nm in volume, surface, and number respectively.

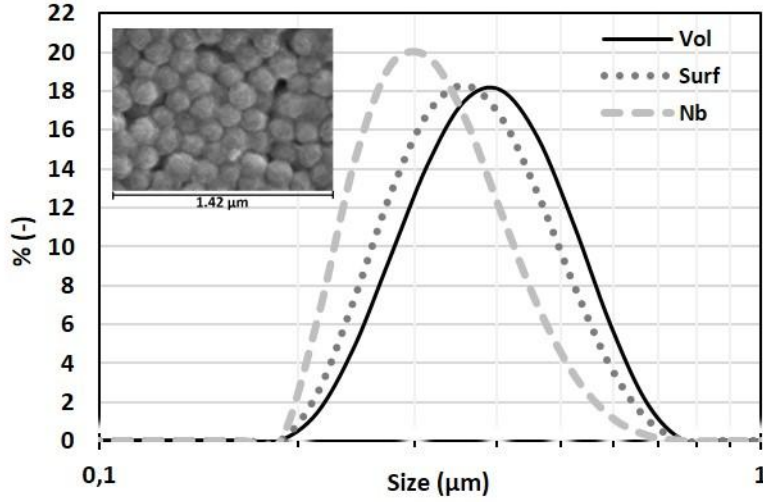


Figure 1 : Volume, surface and number size distributions of the initial MBS nanoparticle suspension and SEM image

All three types of distributions are unimodal with sizes ranging from 0.2 to 0.8 μm. The mode of the volume distribution is 426 nm while the mode of the number distribution is shifted towards the smallest sizes (340 nm) but all three distributions are consistent and characteristic of relatively monodisperse populations. As shown in the SEM photo of the initial MBS latex suspension, inserted in Figure 1, the latex particles have a relatively spherical shape and are fairly similar in size in agreement with the particle size distributions.

Moreover, according to the data provided by laser diffraction, the global fractal dimension [17-18] D_3 can be deduced directly from the negative slope of a log-log plot of the relative scattering intensity (I) versus the modulus of the scattering wave vector (k) given by the following equation where λ is the wavelength and θ the scattering angle:

$$k = \frac{4\pi}{\lambda} \sin \frac{\theta}{2} \quad \#(1)$$

Indeed, in the fractal regime when $R_g^{-1} \ll k \ll r_0^{-1}$ where r_0 is the radius of the primary particles and R_g the radius of gyration of the aggregates, the intensity decays according to a power law which can be defined as the opposite of a scaling factor or fractal dimension D_3 for mass fractal objects [19,20]:

$$I(k) \propto k^{-D_3} \quad \#(2)$$

Image Analysis

An off-line analysis of samples was also performed using Morphologi G3 (Malvern Panalytical®), which is a characterization tool consisting of an optical microscope (coupled to a CDD camera) associated with an image analysis software [12]. For each analysis, a sample is injected between two glass plates separated by a joint in order to reduce the risk of deforming the aggregates and thus biasing the results during image analysis. More than 10000 isolated and digitized aggregates were collected for each sample. From the data provided by the image analysis, the software is able to calculate characteristic shape parameters, such as circle equivalent diameter (CED), circularity and other parameters. In this study, circularity (C) was chosen as a characteristic parameter of the overall shape and surface roughness of the aggregates [12, 21]. It corresponds to the ratio between the perimeter of a circle having the same surface (A) as the projected image of the aggregate and the perimeter (P) of the aggregate:

$$C = 2 \frac{\sqrt{\pi A}}{P} \#(3)$$

Its value varies between 0 for an elongated object to 1 for a disk.

Furthermore, the 2D-fractal dimension (D_2) determined from the results obtained by the image analysis treatment is used to characterize the aggregates [22]. It is determined by the exponent of a relation between the intrinsic area (A_s) and a characteristic length (l_c) of the aggregate:

$$A_s \propto l_c^{D_2} \#(4)$$

The maximum distance, which is the farthest distance between two points of the perimeter, also defined as the maximum Feret diameter, was chosen in this work as the characteristic length of the aggregates. D_2 can take values from 1 to 2 that corresponds to a disk since the area is proportional to the square of the length.

2.2.2 MBS suspension stability analysis

The MBS latex suspension is stable due to electrostatic repulsive forces between the negatively charged particles by the carboxylate group of the potassium salt present on their surfaces. To confirm this, the variation of the zeta potential of the latex suspension was measured as a function of pH by applying the Smoluchowski equation [23] using a Nanosizer ZS (Malvern Panalytical®) (Figure 2). The measurement was performed with a diluted suspension of nanoparticles (0.0215% w) and the pH was adjusted by carefully adding drops of sulfuric acid (15 mmol/l) or sodium hydroxide ($2.5 \cdot 10^{-3}$ mmol/l) to the diluted suspension. For each pH value, the error bars presented in the graph correspond to three different samples, each measured three times to check the stability of the initial product.

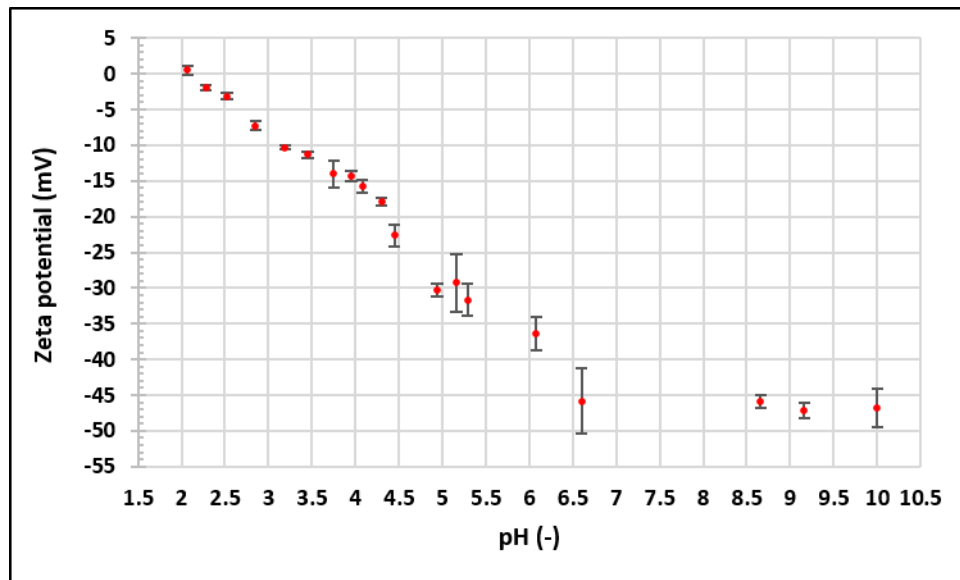


Figure 2: Zeta potential of MBS latex suspension versus pH

According to the DLVO theory, the higher the potential, the better the stability. The zeta potential of the diluted suspension (pH \approx 6) is -35 mV which confirms its good stability ($|\text{zeta}|$ being higher than 30 mV) [24]. In basic medium, the zeta potential increases to reach constant values of -48 mV beyond pH=8.5. In acidic medium, the absolute value of the zeta

potential decreases to zero around pH=2. This observation reflects the fact that particles can aggregate under acidic conditions.

2.2.3 MBS suspension density

Measurement of the change in density of the MBS latex suspension with temperature was performed using an oscillating tube density meter (Anton PAAR DMA 4100M). The values measured for a 21.5%w suspension are presented in the supplementary material (see Figure S1). The evolution of density with temperature is similar to that of water although lower values than water were measured over the entire temperature range considered. The density of the suspension as a function of temperature (T) can be described by the following equation:

$$\frac{\rho}{\rho_0} = 0.7205 + 0.59 \frac{T}{T_0} - 0.3105 \left(\frac{T}{T_0} \right)^2 \quad (5)$$

where ρ is the density and $\rho_0=0.9974 \text{ g/cm}^3$ the density at $T=0^\circ\text{C}$ and $T_0=273.15\text{K}$.

2.2.4 MBS suspension rheological behaviour

The rheological behavior of an MBS latex suspension was measured at room temperature using a rotational rheometer (Kinexus pro+ Malvern Panalytical®) with a double-gap geometry that consists of filling the sample into a double cylinder when a second cylinder is lowered into it to create different shears on the fluid. The suspension behaves as a shear thinning fluid as shown in Figure S2. The rheological data from 1 to 500 s^{-1} were fitted to the Cross model (see Figure S2) relating apparent viscosity (μ) to shear rate ($\dot{\gamma}$) according to the following equation:

$$\mu = \mu_\infty + \frac{\mu_0 - \mu_\infty}{1 + (c\dot{\gamma})^m} \quad \#(6)$$

Where assuming the zero-shear viscosity $\mu_0=0.012 \text{ Pa.s}$ and the infinite viscosity at very high shear rates $\mu_\infty=0.0011 \text{ Pa.s}$, we obtain $c=1.41$ the consistency coefficient and $m=0.84$ the rate constant reflecting the degree of dependence of the viscosity on the shear rate.

2.2.5 Thermomechanical properties

The thermomechanical properties of the core-shell MBS copolymer aggregates were evaluated by Dynamic Mechanical Analysis (DMA). This technique was chosen because it is widely used to characterize thermomaterial properties as a function of temperature, time, frequency, stress, atmosphere or a combination of these parameters [25]. DMA applies an oscillatory force at a specified frequency to the sample and reports changes in stiffness and damping that can be expressed in terms of ($\tan \delta$) defined as the ratio of loss and storage modulus. This type of analysis cannot be performed directly on a solid-liquid suspension. For this purpose, the suspensions were filtered and then dried in a fluidized bed at a temperature of 50°C . The powder obtained was pressed to form a disk of 1.71mm thickness and 5mm diameter. Two disks were mounted in the shear clamp and analyzed with a Metler Toledo DMA 1. The heating was from -100°C to 180°C at 3K/min based on results in literature [2, 26]. Measurements were performed in a frequency series at 10 and 1 Hz to determine the glass transition of MBS aggregates which corresponds to the temperature range where a polymer changes to a softer and more compliant state. It can be determined when the maximum of ($\tan \delta$) occurs.

2.3 Experimental Setup and protocol

Aggregation experiments were performed in a 1-liter jacketed and cylindrical batch reactor equipped with four long and flat baffles. A scheme is presented in Figure 3.

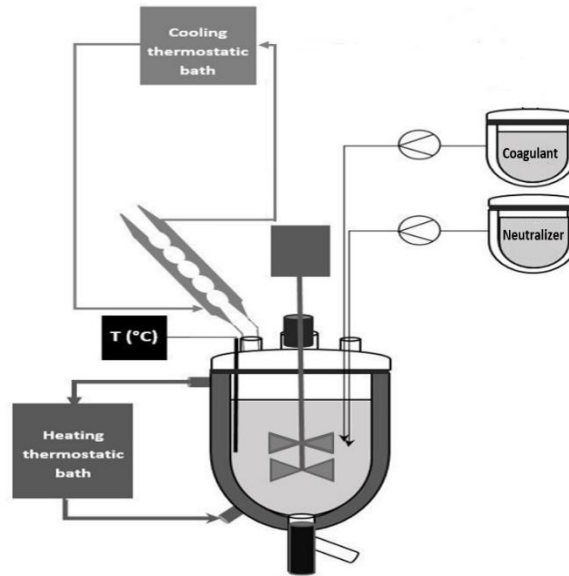


Figure 3: Scheme of the experimental set-up for MBS aggregation experiments

Two superposed propellers (BOHLC443-08), commercialized by BOLA Rührwellen, were used in all experiments presented in this article. They are fixed on a 10 mm shaft in the center of the tank and separated by a distance of 60 mm. Their diameter is 60 mm and the distance between the lower propeller and the bottom of the tank is 18 mm. Each propeller consists of four blades made entirely of PTFE and inclined at 45° to achieve good axial flow with low shear force. A thermostatically controlled silicone oil bath controls the temperature of the suspension by circulating the cooling or heating fluid through the jacket around the vessel. Moreover, a bulb condenser consisting of a long glass tube with a water jacket allows the condensation of the vapors produced during the process. The evolution of the process at different steps can be followed by taking samples through an outlet located at the bottom of the reactor.

Latex aggregation runs were performed according to a specific protocol (Figure 4) derived from the coagulation process of the core shell polymer cited in a patent specification deposited by ARKEMA [16].

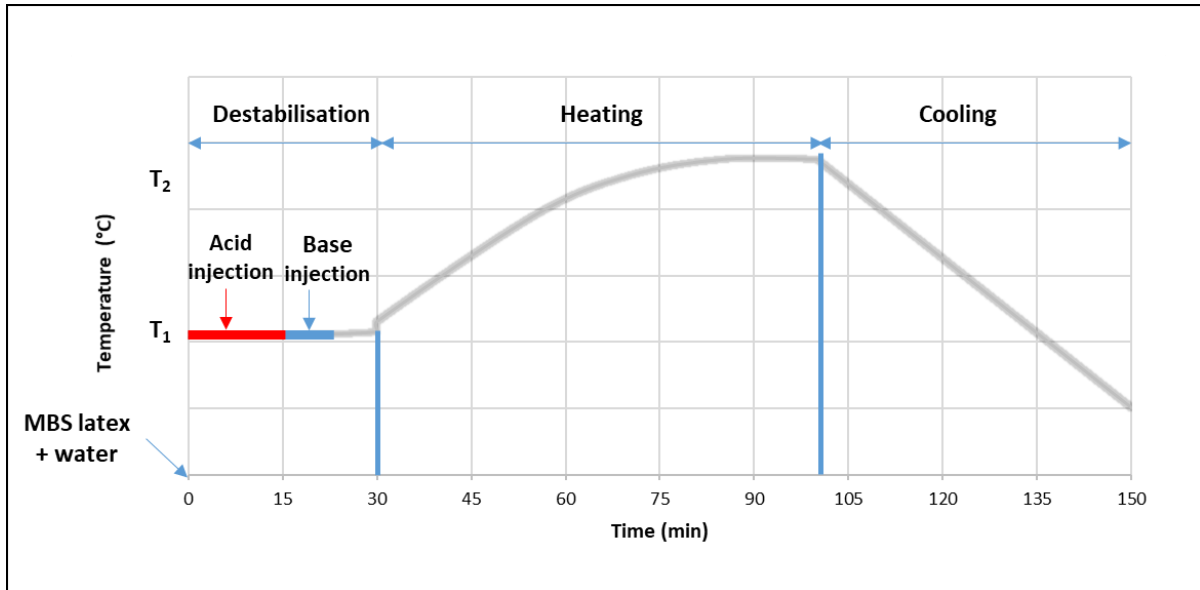


Figure 4 : Experimental protocol

First, a 500 ml latex suspension, diluted to 2.15%w with demineralized water, is introduced into the reactor. Stirring is set at $N=200$ rpm or 450 rpm and the temperature of the suspension is raised up to T_1 (20, 30 or 42°C). A 215 ml solution of a sulfuric acid prepared at a specific concentration (7.5, 15 or 30 mmol/l) is injected into the reactor by a peristaltic pump at a flow rate of 0.23 ml/s (duration : 16 minutes). Then 60 ml of a sodium hydroxide solution is added at the same flow rate to obtain a neutral pH (around 6 or 7). Hence, the total volume in the reactor is equal to 775ml and the concentration of the acid corresponds to 2.08, 4.16 (denoted C_a) or 8.32 mmol/l. The reactor temperature is then raised to T_2 (42, 60, 80 or 95°C) and maintained for 30 min. At the end of the run, the mixture is cooled to ambient temperature.

In this paper, the influence of the coagulant concentration, the stirring rate and the temperatures of the two steps of the protocol (T_1) and (T_2) on the size and shape distributions of the agglomerates was studied. Table 1 summarizes the operating conditions of each experiment.

N°	Acid Concentration	T_1 (°C)	T_2 (°C)	N (rpm)
1	C_a	42	95	200
2	$2 C_a$	42	95	200
3	$C_a/2$	42	95	200
4	C_a	20	95	200
5	C_a	30	95	200
6	C_a	42	42	450
7	C_a	42	60	450
8	C_a	42	80	450
9	C_a	42	95	450

Table 1 : Experimental conditions for aggregation runs

3. Results and discussion

3.1 Morphological changes during the aggregation process

Before analyzing the effect of the different parameters on the evolution of the size and shape distributions, the results of Exp #1 are first presented and discussed. Table 2 reports the modes (most probable sizes) and median diameters of the initial suspension and at the end of the acidic destabilization and heating steps during which aggregation occurs, Figure 5 shows the corresponding volume, surface and number size distributions.

Phase	Volume		Surface		Number	
	Mode (μm)	Median (μm)	Mode (μm)	Median (μm)	Mode (μm)	Median (μm)
Initial	0.43	0.41	0.38	0.38	0.34	0.34
Destabilization	81.2	56.3	10.53	14.8	2.28	3.73
Heating	376	387	331	336	256	262

Table 2 : Mode and median diameters of the initial suspension and at the end of the destabilization and heating steps

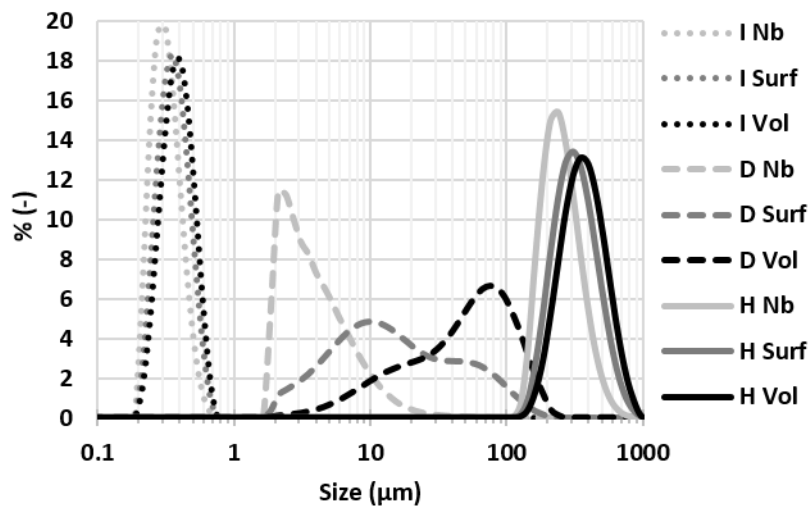


Figure 5 : Number, surface and volume size distributions of the initial suspension I (dotted lines), at the end of the destabilization step D (dashed lines), and at the end of the heating step H (continuous lines) – Exp #1

Destabilization Step

Under these reference conditions (Exp #1), the distribution starts to evolve from the first drops of acid addition until it reaches a constant distribution after the addition of 100 ml (get at 7 min) of sulfuric acid which leads to a pH close to 2. Indeed, it is the pH obtained during that step that controls the aggregation phenomenon. When an acidic medium (pH=2) is obtained by adding sulfuric acid, the zeta potential becomes almost zero (see Figure 2). As a result, the repulsive electrostatic forces are reduced compared to the attractive Van der Waals forces, which leads to the aggregation of the latex nanoparticles according to the DLVO theory.

During the rest of the destabilization step, the size distributions do not evolve anymore. Hence, in relation to Figure 2, it can be stated that the amount of coagulant is more than sufficient to completely destabilize the suspension. The main aggregation phenomenon is the charge neutralization, which is quite rapid. These “intermediate aggregates” have a wider and larger size range than the primary particles. It can be stated that the size distributions are broad. The volume distribution of aggregates ranges from 2 to 200 μm represented by a distribution with a streak on the left emphasizing the presence of some small flocs. While for

the number representation, the range is more shifted to the left between 1.8 and 30 μm indicating the presence of most small flocs. Furthermore, the surface distribution can be considered as an intermediate between these two representations. As a consequence, the aggregation population is quite large and heterogeneous as it is mainly composed of numerous small aggregates of about 2 μm and larger aggregates with sizes up to 200 μm ; the span of the sizes being spread over 2 decades.

Neutralization step

During the neutralization step, the distributions (not shown here) remain stable. Thus, after neutralization, the pH of the suspension has no more effect on the aggregation phenomenon.

Heating step

The second phase of aggregation takes place during the temperature rise. The size distribution gradually evolves with temperature until a steady-state distribution is reached when the temperature is equal to $T_2=95^\circ\text{C}$. After that, the aggregate size distributions do not evolve, even if the suspension remains at T_2 for a long time. The size distributions are not affected by the cooling phase. The volume size distribution determined by laser diffraction is unimodal with sizes ranging from 130 to 1000 μm . The heating step therefore leads to the formation of very large aggregates. Similarly, the surface distribution shows the same range with a small left shift of the peak. While the number representation shows a size range between 110 and 900 μm with a more left-shifted peak. It can be noticed in Figure 5 that the overall population at the end of the heating step is much more homogeneous in terms of sizes than that at the end of the destabilization step. In Table 2, the mode and median diameter are close to each other.

The evolution of the fractal dimension D_3 of latex aggregates is plotted in Figure 6 as a function of temperature.

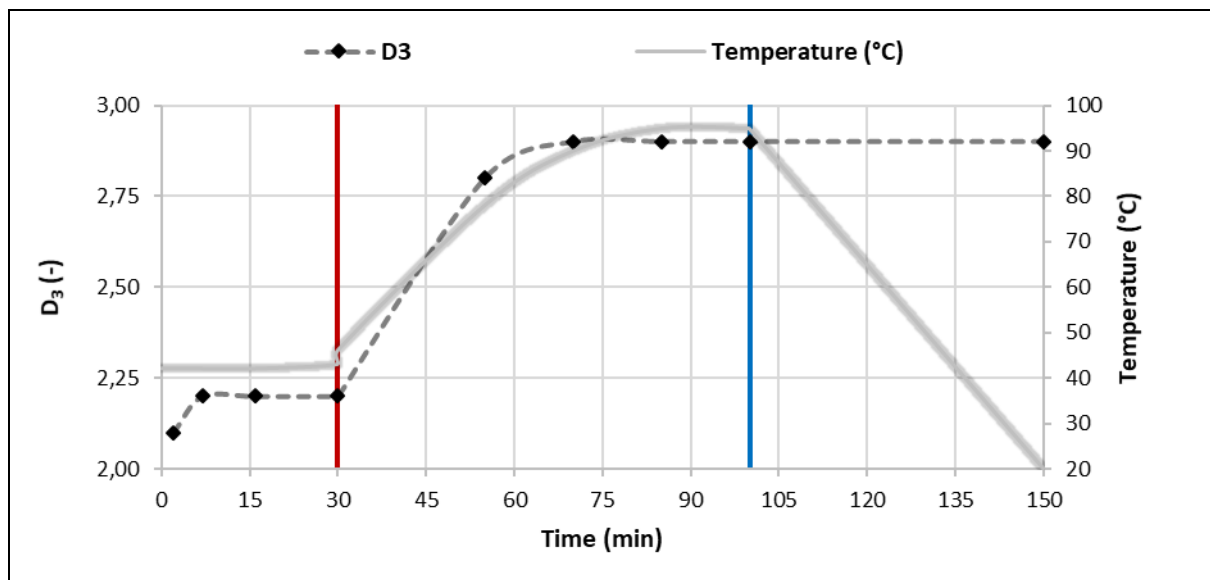


Figure 6 : Fractal dimension D_3 and Temperature versus time – Exp #1

For the initial suspension, the fractal dimension has no physical significance because the first aggregates formed cannot be considered as fractal objects [10, 15, 27]. Thus D_3 was measured only a few minutes after the start of the acid injection. During the sulfuric acid injection (which lasts 16 minutes), the D_3 increases slightly with the size of the aggregates. The further increase of the fractal dimension until the end of the destabilization step may be related to a kind of compaction of the aggregates that has already been underlined in the literature. At the

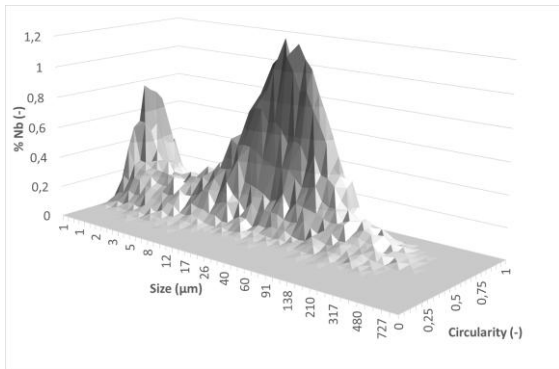
end of the destabilization step, we obtain aggregates with a fractal dimension of about 2.2; value consistent with those found in the literature [8, 13, 28-30]. This value continued to evolve during the heating step to reach a final value of 2.9 at 95°C, reflecting that the aggregates become denser.

From the analysis of the images provided by the Morphologi G3, it is possible to determine the distribution of basic morphological characteristics of more than 10000 aggregates collected for each sample. To represent the morphology of the whole population, a 3D graph is proposed [12]; on the same graph is presented the distribution according to the aggregate size and the circularity. This representation allows highlighting the relationship between the size and the shape of the aggregates. An example is shown in Figure 7 for the number and volume distributions of size and circularity at the end of the destabilization and heating steps for Exp #1.

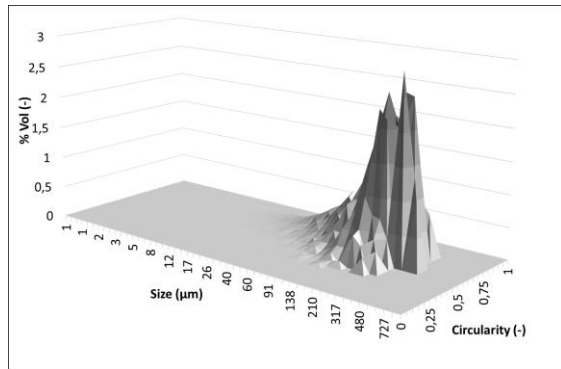
After the addition of acid, the number distribution (Figure 7.a) shows that two different populations appear: (i) a population of primary aggregates with a size between 1 and 10 μm with a mean circularity of 0.68 and (ii) a population of larger aggregates with a size between 10 and 300 μm with a mean circularity of 0.76 while the volume distribution (Figure 7.b) shows aggregates between 40 and 500 μm with a mean circularity of 0.73. It should be remembered that, in contrast to laser diffraction measurements, the data from image analysis are natively in numbers and then transformed to obtain the volume distributions. We observe here that the population, highlighted by the volume distribution corresponds in fact to very few large aggregates. Overall, these graphs indicate that during the destabilization step, the particles form primary aggregates with low circularity values before these coalesce to form intermediate and more circular aggregates. After the heating step, the number distribution (Figure 7c) shows a first sub-population between 1 and 200 μm with an average circularity around 0.8. This sub-population is a part of the aggregates formed during the destabilization step that did not aggregate during the second heating step. But the main population is constituted by much larger aggregates between approximately 200 and 900 μm with a mean circularity of 0.83. This second population of quite large and circular aggregates is well put in evidence in the volume distribution (Figure 7d). Moreover, this observation is also in agreement with the volume size distribution determined by laser diffraction and reported previously in Figure 5, suggesting that a monodisperse population is finally recovered at the end of the heating step. As for the number size distribution, also shown in Figure 5, as already mentioned in the introduction, it is calculated from the volume distribution and may therefore not highlight the presence of a few small aggregates detected by image analysis. Both analysis methods (laser diffraction and image analysis) provide complementary data, and analysis of the results interpreted on the basis of number and volume distribution sheds new light.

The 2D fractal dimension, deduced from the image analysis, evolves little, from 1.86 after the destabilization step to 1.99 after the heating step, but it confirms the formation of very circular aggregates.

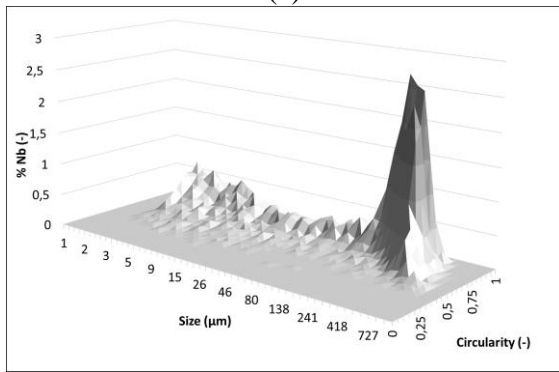
Thus, it can be stated that the final aggregates formed after heating are larger and more circular than those obtained after the destabilization step. Indeed, the small aggregates obtained spontaneously by the addition of coagulant tend to aggregate over time, under the effect of heating, to form more circular aggregates. These observations are also supported by images of the aggregated suspensions recovered at the end of the destabilization step and at the end of the heating step and reported in Figures 7e and 7f respectively. In addition, a selection of images of aggregates is shown as supplementary material in Figure S3.



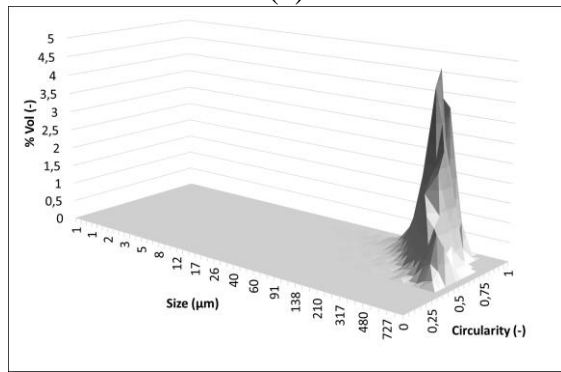
(a)



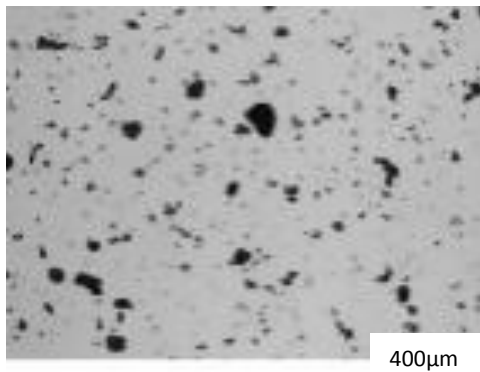
(b)



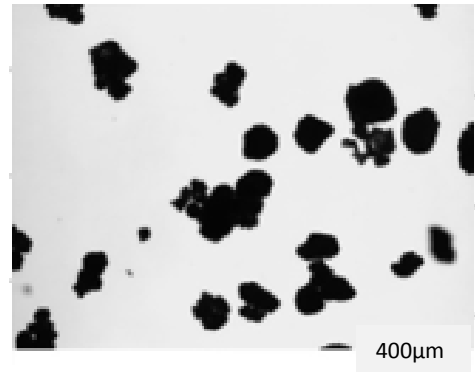
(c)



(d)



(e)



(f)

Figure 7 : 3D distribution of size and circularity – Exp # 1.
 a) Number and b) Volume distributions at the end of the destabilization step.
 c) Number and d) Volume distributions at the end of the heating step
 (e) Image of the aggregated suspension recovered at the end of the destabilization step
 (f) Image of the aggregated suspension recovered at the end of the heating step

This evolution of the latex according to the different steps of the protocol was observed in all the experiments performed. Indeed, whatever the physicochemical and hydrodynamic conditions applied during the experiment, we can distinguish two main aggregation phases : the coagulation phase which corresponds to the destabilization by the addition of sulfuric acid

and a subsequent aggregation phase during the heating step. Moreover, once the aggregation is achieved, the aggregates do not change with time, which implies that the two aggregation phenomena mentioned above are fast, permanent and irreversible.

3.2 Factors influencing aggregation

Stirring speed

The effect of the stirring speed on the aggregate size can be analyzed by considering Exp #1 and Exp #9. These experiments were performed with the same concentration of acid, T_1 and T_2 , only the rotation speed (N) of the stirrer was different: 200 rpm for Exp #1 and 450 rpm for Exp #9. By comparing the distributions of Exp #1 and Exp #9, it can be noted that the mode of the distribution depends on N (it is equal to 352 μm for $N=200$ rpm and 211 μm for $N=450$ rpm). A number of studies [31-36] show that there is a relationship between the aggregate size and the turbulence scales. The ratio of the Kolmogorov microscales for Exp #1 and Exp #9 can be estimated by the following equations :

$$P_w = N_p \cdot \rho \cdot N^3 \cdot D^5 = \frac{\varepsilon}{\rho \cdot V} \quad (7)$$

and

$$\eta = \left(\frac{\nu^3}{\varepsilon} \right)^{\frac{1}{4}} \quad (8)$$

giving

$$\frac{\eta_{Exp\#1}}{\eta_{Exp\#9}} = \left(\frac{N_{Exp\#9}}{N_{Exp\#1}} \right)^{3/4} \cong 1.8 \quad (9)$$

Where P_w is the supplied and dissipated power, N_p the power number of the impeller, ρ the suspension density, N the stirring speed, D the impeller diameter, ε the volume average of the viscous dissipation of the kinetic energy, V the volume of liquid in the reactor, η the average Kolmogorov microscale, and ν the kinematic viscosity of the suspension.

This ratio can be compared to the ratio of the modes of the volume distributions ≈ 1.7 . Both ratios are quite similar, indicating that even in the case of a heating step, the agglomeration phenomena seem to be closely related to hydrodynamics.

Coagulant concentration

The effect of coagulant concentration was examined while keeping the other experimental conditions constant and can be analyzed by referring to Exp #1 Exp #2 and Exp#3. To avoid variation in the total reactor volume, 215ml sulfuric acid solutions at different concentrations were used to destabilize the latex suspension. Figure 8 shows the size distribution for three experiments with an acid concentration of 2.08, 4.16 and 8.32 mmol/l (denoted $C_a/2$, C_a , $2 \cdot C_a$) at 2 minutes, 7 minutes and 16 minutes after the start of sulfuric acid injection (during the destabilization step), respectively.

The kinetics of the destabilization step is affected for low coagulant concentration. Indeed, the size distribution of the aggregates shows a similarity between the three experiments after 7 min (Figure 8.b) and at the end of the destabilization step (Figure 8.c). While after 2 min of

addition (Figure 8.a) the suspension is not yet coagulated for $C_a/2$ which is particularly shown by the peak of number distribution between 0.2 and 0.9 μm . In volume representation, this can be noticed by the presence of a minor peak at this size range. This implies that the amount of coagulant added is not yet sufficient. In agreement with this observation, the number median diameter for $C_a/2$ evolves from 0.34 μm for the initial suspension to 0.45 μm after 2 min, then to 3.5 μm after 7 min which remains almost fixed until the end of the destabilization step. While for C_a or $2.C_a$, the number median diameter is already 3.5 μm after 2 min, but remains around 3.9 μm at the end of the step. The variation of the acid concentration has no persistent influence on the aggregates formed after heating (not shown here). Similarly, it was observed that it does not affect the global fractal dimension determined by laser diffraction. Its value changes from 2.1 after the destabilization step to 2.7 after the heating step, as shown in Figure 6.

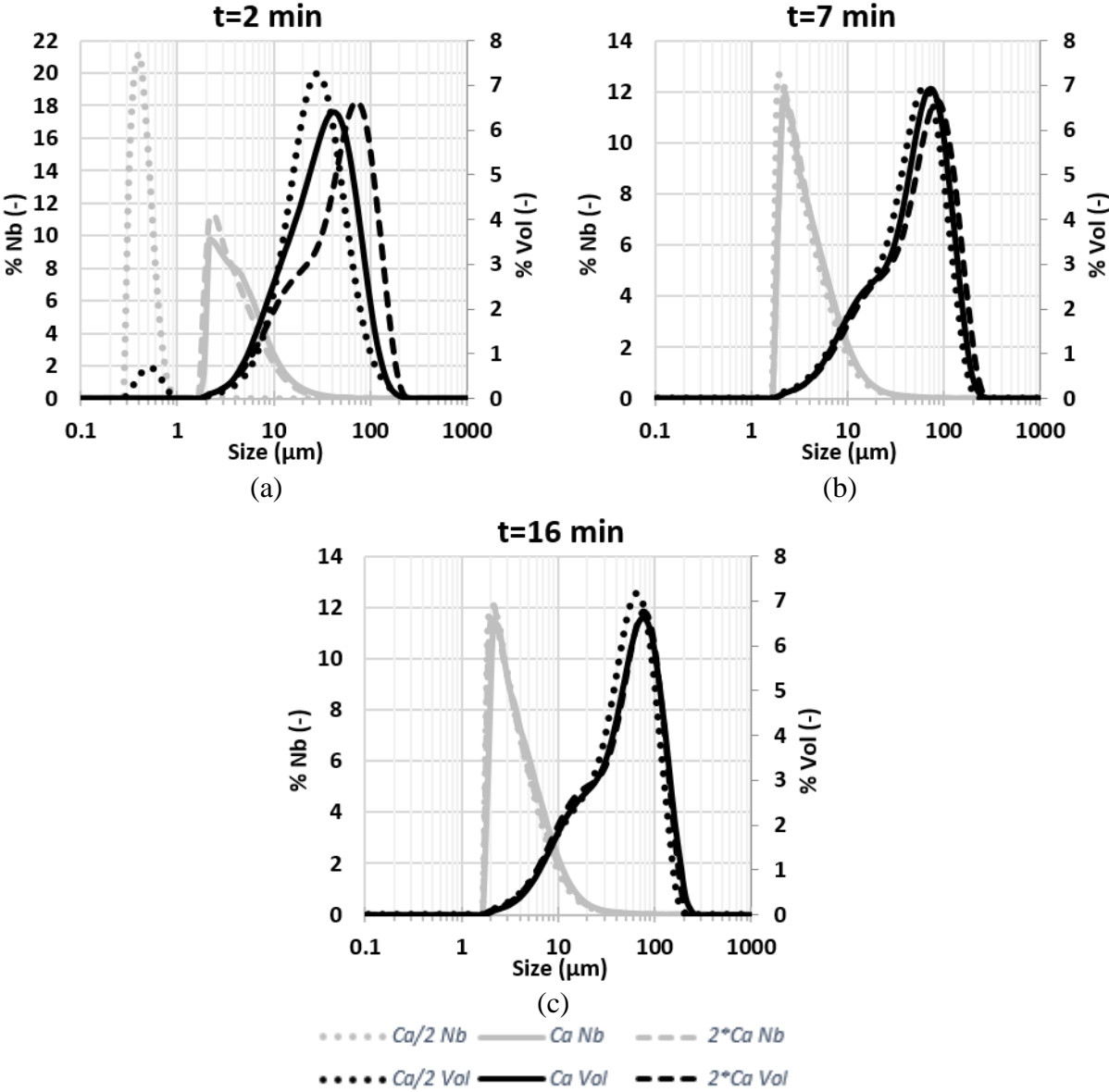


Figure 8: Number and volume size distributions during the destabilization step for different acid concentrations (Exp #1, Exp #2, Exp #3). (a) $t=2\text{min}$, (b) $t=7\text{min}$, (c) $t=16\text{min}$.

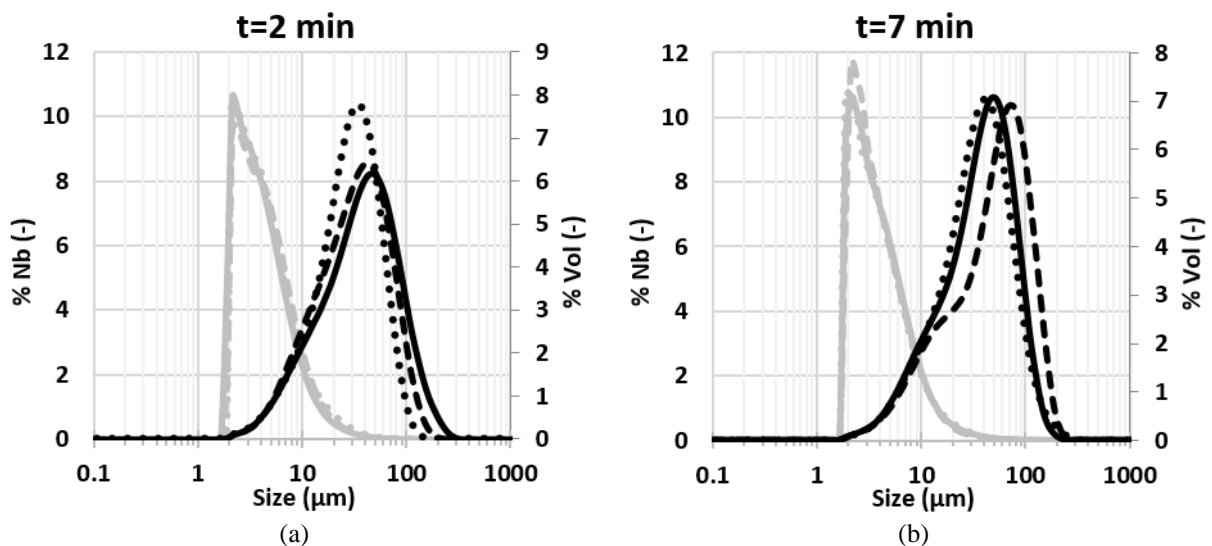
These experiments prove that the acid concentration does not affect the size or morphology of the intermediate and final aggregates as long as the rate of acid injection is moderate and the amount of acid is sufficient to achieve a low pH corresponding to negligible zeta potential values.

Destabilization temperature T_1

The influence of temperature during the destabilization step can be discussed by referring to Exp #1, Exp #4 and Exp #5.

In the graphs in Figure 9, the volume and number size distributions at different times of the destabilization step are given for the aggregates of three different experiments performed with destabilization temperatures T_1 of 20°C, 30°C, and 42°C, respectively. Note that regardless of the temperature, approximately the same size distributions are obtained at each time point during the destabilization step. The number distributions at the end of the destabilization step vary between 1.8 and 30 μm represented by a monomodal distribution with a peak at 2 μm and a streak on the right emphasizing the presence of fewer aggregates between 10 and 30 μm . The volume representations show the presence of aggregates between 2 and 200 μm from the beginning of the injection and regardless of the temperature of the destabilization step. Nevertheless, it can be noticed that the kinetics of the onset of aggregation seems to be somewhat affected by temperature. Indeed, in the Figure 9.a, the higher the temperature, the greater the distribution mode. At the end of the destabilization step (Figure 9.c), the mode of the volume distribution is slightly shifted to the right for a temperature of 42°C.

Similarly to the sulfuric acid concentration, no effect of the destabilization step temperature on the fractal dimension was observed. The temperature of the first aggregation phase has no significant effect on the size and morphology of the aggregates.



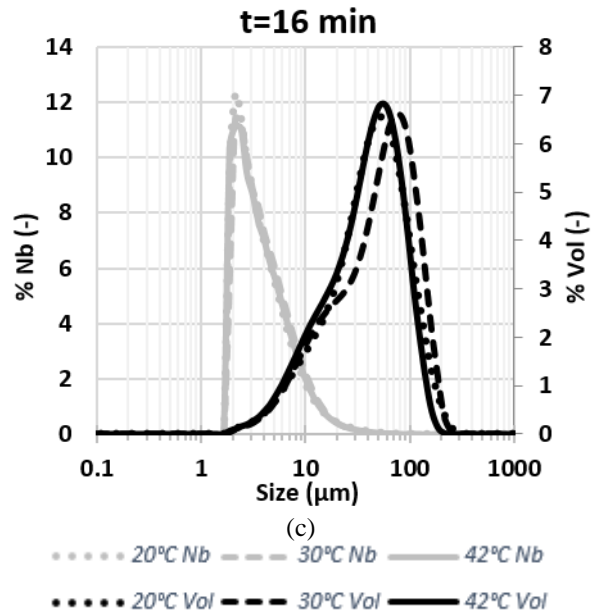


Figure 9: Number and volume distributions during the destabilization step for different T_1 (Exp #1, Exp #4 and Exp #5). (a) $t=2$ min, (b) $t=7$ min, (c) $t=16$ min.

Heating temperature T_2

The effect of the temperature of the heating step can be analyzed by referring to Exp #6 to Exp #9. Note that for these 4 experiments, the destabilization step was performed at a temperature of 42°C ; with a concentration of C_a sulfuric acid and a rotation speed of 450 rpm. The volume and number size distributions are presented in Figure 10 for the four experiments performed at T_2 of 42°C, 60°C, 80°C and 95°C respectively.

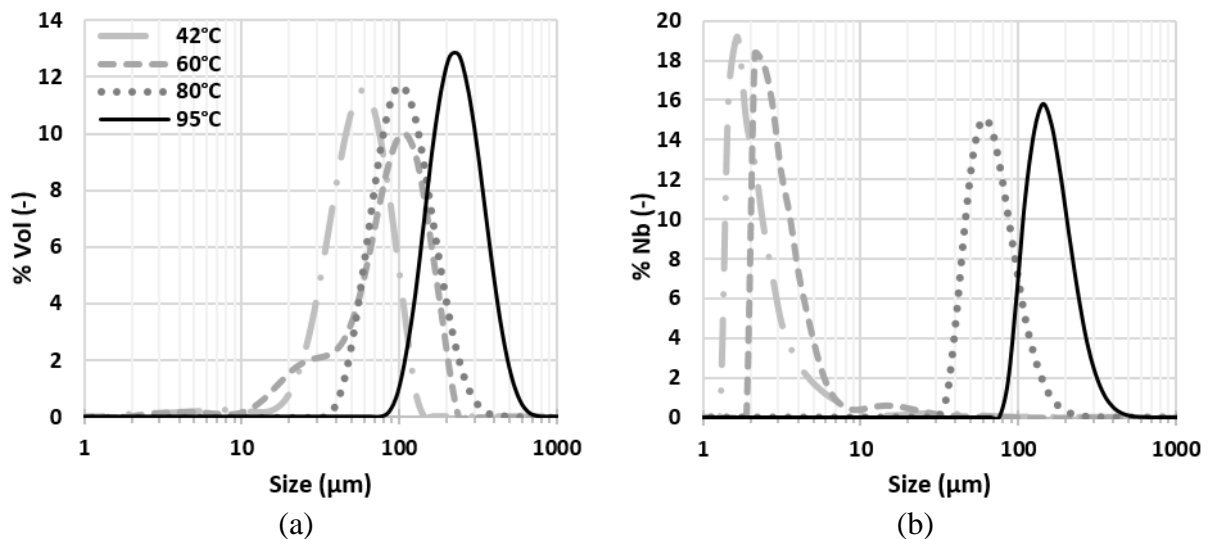


Figure 10: Volume (a) and number (b) size distributions at the end of the heating step for different T_2

Heating Temperature	Volume		Surface		Number	
	Mode (μm)	Median (μm)	Mode (μm)	Median (μm)	Mode (μm)	Median (μm)
42°C	62.9	58.9	48.7	41.1	1.77	2.1
60°C	119	95.3	92.25	35.9	2.28	3.1
80°C	104.55	112	92.25	93.7	62.9	70.7
95°C	225.5	244	198.5	211	153.5	165

Table 3 : Mode and median diameters at the end of the heating step for different T_2

When the temperature is maintained at 42°C during the heating step, the volume representation (Figure 10.a) shows a monomodal distribution between 20 and 120 μm with a small fraction of smaller aggregates below 10 μm . While for the number representation (Figure 10.b), the peak is even more shifted to the left revealing that the majority of the aggregates are smaller than 10 μm in size. These distributions are similar to those obtained at the end of the destabilization step but they are narrower, i.e. fewer large aggregates ($>10\mu\text{m}$) are observed in the number representation and fewer small aggregates ($<10\mu\text{m}$) in the volume representation. When heated to 60°C, the volume distribution starts to shift to the right as the mode is close to 100 μm , but a significant portion of small aggregates between 10 and 50 μm is noticeable. Looking at the number distribution, it is obvious that there is still a large portion of the population with sizes between 2 and 10 μm . It can also be noticed that increasing the heating temperature from 42 to 60°C leads to a slight change in the size of the smallest aggregates.

Looking at the results for $T_2= 80^\circ\text{C}$, the volume distribution shows a range close to that of heating at 60°C but with the disappearance of the smallest flocs between 10 and 50 μm , while the number distribution shows that the aggregates are significantly larger ($>30\mu\text{m}$), the mode of the distribution being close to 60 μm . For $T_2=95^\circ\text{C}$, the aggregates are even larger either in number or in volume. Indeed, the size range is between 90 and 700 μm in volume representation and between 80 and 600 μm in number representation. In summary, it is clear that the higher the temperature, the larger the aggregates. Moreover, the size distribution becomes narrower with increasing temperature and the number and volume distributions become closer together.

Let us now consider the fractal dimensions of the latex aggregates. The 2D fractal dimension was determined from image analysis according to (Eq. 4) and the 3D global fractal dimension was deduced from laser diffraction measurements (Eq. 2). The determination of the 3D global fractal dimension in the fractal regime from laser diffraction measurements for the different runs varying the temperature of the heating step is reported in supplementary material (see Figure S4). Although correlations have been developed in the literature [37,38] to link 2D and 3D fractal dimensions, and thus predict for example the 3D fractal dimension from 2D images, it seems difficult here to directly compare volume fractal dimensions, obtained by laser diffraction of one part and calculated from 2D analyzes of another part, knowing that the values come from experimental data based on very different physical principles. However the evolution of 2D and 3D fractal dimensions follow similar trends. The correspondence between temperature changes and 2D or 3D fractal dimensions of the flocs can be seen in Figure 11.

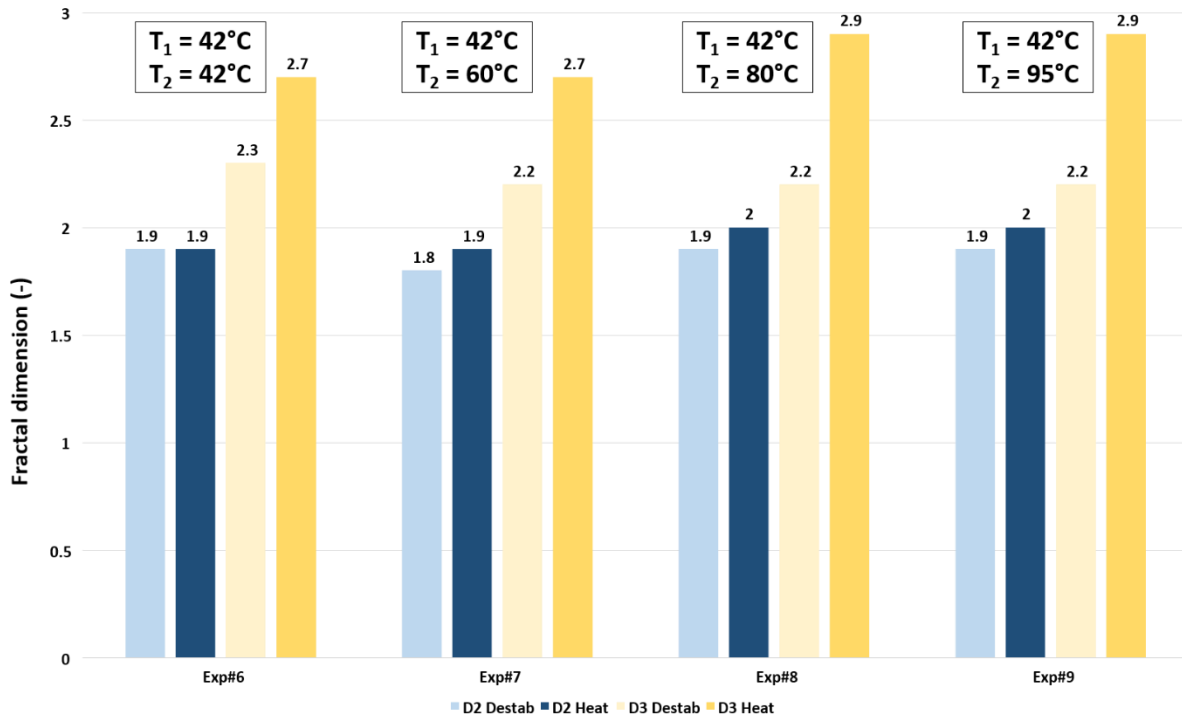


Figure 11: D_2 and D_3 fractal dimensions versus Temperature (Exp. # 6 to Exp #9)

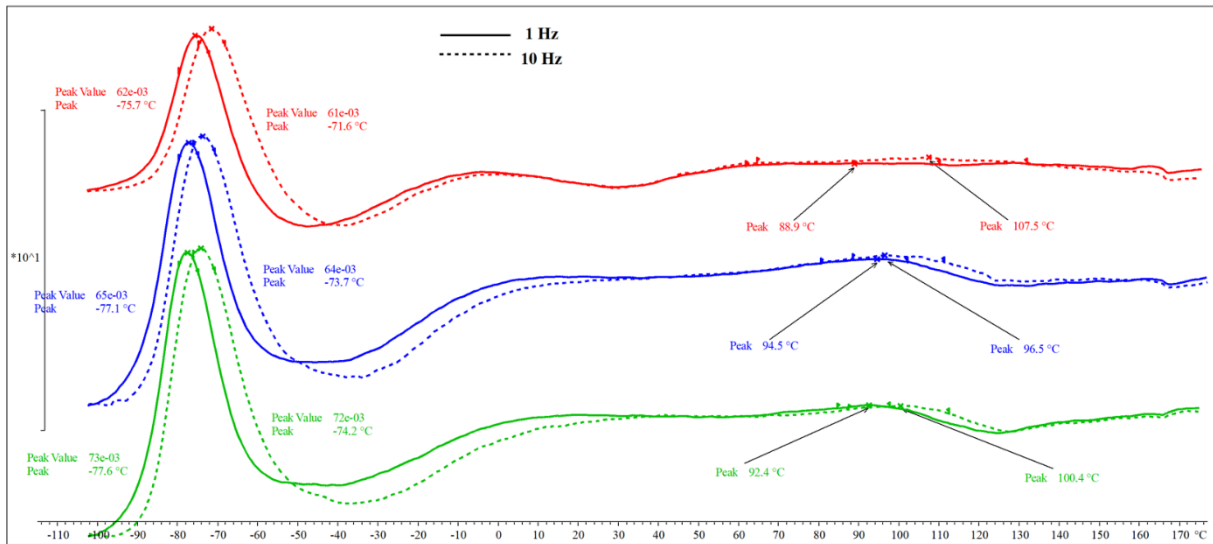
Remember that the range of variation of 2D and 3D fractal dimensions is not the same, depending on their respective definitions. The 2D fractal dimension varies between 1 (for a line) and 2 (for a disk), while the 3D fractal dimension varies between 1 (for a needle) and 3 (for a sphere). Despite this, the same evolutionary trends as a function of temperature were observed. After the destabilization step, performed at 42°C for Exp #6 to Exp #9, the 2D fractal dimension is on average equal to 1.9 and the D_3 fractal dimension to 2.2. After the heating step, the 2D fractal dimension becomes almost equal to 2 (maximum value) and D_3 reaches 2.9 for the highest heating temperatures (80°C and 95°C). It is slightly lower (2.7) if the heating step is performed at 42°C or 60°C. Thus, the fractal dimension increases slightly if the temperature of the second step is the same as that of the destabilization step (case of Exp #6). This increase, as indicated above, is accompanied by a slight narrowing of the distribution. We can think that the largest aggregates maintained under agitation at constant temperature undergo a slight erosion. Finally, from these results, it can be assumed that the larger aggregates have higher fractal dimension values, or that increasing the temperature leads to the formation of larger, but denser aggregates.

In summary, the heating step, when performed at high temperature, leads to an efficient agglomeration phase since it allows the formation of a population of large, dense and relatively circular aggregates. To our better knowledge, there are only a few articles in the literature [1, 14] mentioning the influence of temperature on the agglomeration efficiency. In order to better understand the underlying mechanisms, DMA analyses were performed on the agglomerates after the destabilization and heating steps.

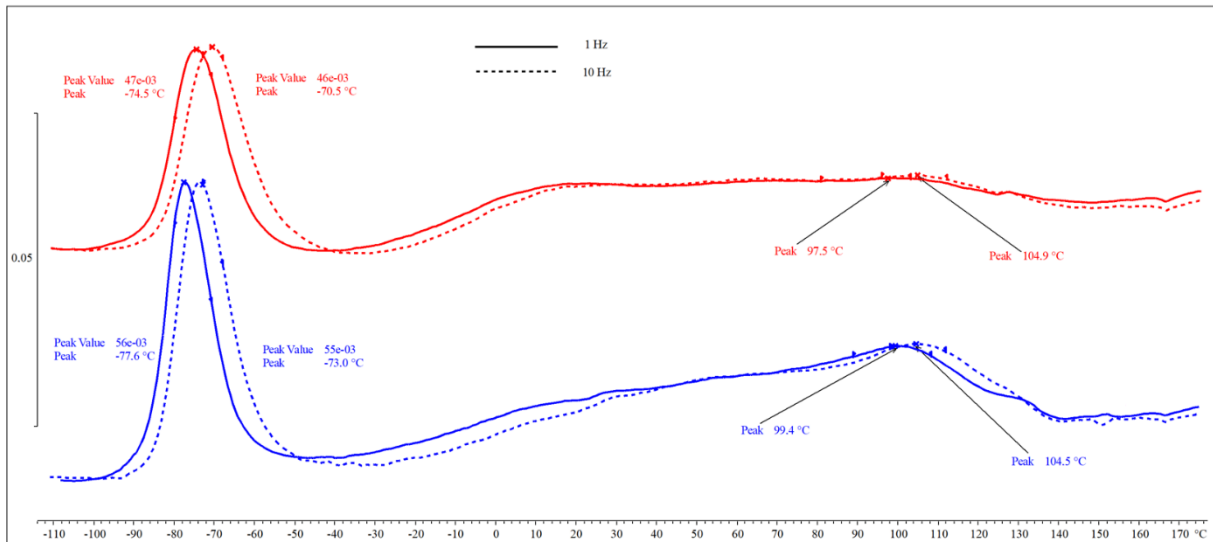
The DMA results for the aggregates obtained in experiments with different heating temperatures (42°C and 95°C) are presented in Figure 12. The heating cycles were repeated several times: the first and second heating are represented by the red and blue line for both

samples (42°C and 95°C), respectively, and the third heating is represented by the green line performed only for the sample obtained at 42°C. In dotted lines, are reported the curves realized at 10 Hz and in solid lines, the curves realized at 1Hz. The determination of the different transitions of MBS copolymer is based on the results of the literature [2, 26].

From Figure 12, a first phenomenon, weakly dependent on the frequency of sollicitation, is detectable around -75°C for both samples at different heating cycles and may correspond to the alpha transition of the polybutadiene. At about 20-40°C, the frequency curves overlap, probably indicating crystallization of the polybutadiene. Around 95°C, a second phenomenon, corresponding to the alpha transition of methyl methacrylate, is evident for both samples. It is frequency dependent and is particularly noticeable during the second heating cycle (blue line) due to a separation of the butadiene/metacrylate zones that occurred during the first cycle. If we compare the two samples, we notice that the height of the peak is greater for the aggregates obtained at 42°C than for those at 95°C in the first pass, whereas in the second pass, the values are approximately the same. This implies that after the heating step of the aggregation process, the aggregates are more constrained and therefore less damped. In summary, the DMA results indicate that the core-shell MBS particle consists of a nuclear layer, i.e., a core with a glass transition temperature of -75 °C, and a shell with a T_g of approximately 95 °C - 100 °C. This is consistent with previous reports [2, 26]. These transitions indicate subtle changes in the material. The glass transition T_g being the temperature range where the material softens, we can assume that agglomeration phenomena are promoted as soon as the temperature approaches T_g allowing the formation of large and dense aggregates. Therefore, the higher the temperature of the heating step, the larger the aggregates formed. This coincides with what is found in the literature [14]; when T_g is exceeded, the polymer is more "sticky", which facilitates penetration between the chains of colliding particles. Glass transition agglomeration is a common process in fluidized bed spray agglomeration processes [39-41] where particles, being wetted by a liquid, collide at wet spots; the material becoming sticky if the process temperature is close to the glass transition temperature. Solid bridges can finally be created, leading to the formation of agglomerates during drying contrary to the agglomeration process in liquid suspensions. A few papers [42-43] address the effect of particle agglomeration and interphase on the glass transition temperature of polymer nanocomposites but they are mostly devoted to thin polymer films and not, as in our case, for suspended MBS nanocomposites, i.e. closer to industrial aggregation conditions.



(a)



(b)

Figure 12: DMA results - Tangent Delta versus Temperature ($^{\circ}\text{C}$) for 2 experiments with different heating temperatures: (a) $T_2=42^{\circ}\text{C}$ and (b) $T_2=95^{\circ}\text{C}$

4. Conclusions

Aggregation experiments of MBS latex particles were performed in a laboratory-scale stirred reactor according to a specific two-step protocol (destabilization and heating steps) derived from the industrial core-shell polymer coagulation process. The results have shown that two aggregation mechanisms occurred successively: particle destabilization by charge neutralization due to sulfuric acid addition and aggregate consolidation during the heating process. During destabilization step, sulfuric acid acts on the negatively charged surface of the latex particles and leads to the reduction of the potential barrier, which leads to a preliminary aggregation phase. During the heating step, the evolution of the aggregate size distribution and the fractal dimension D_3 derived from the laser diffraction analysis shows that the aggregates formed are larger and larger and their circularity increases. This suggests that

small aggregates are built by a particle-cluster mechanism, whereas large agglomerates are formed by the aggregation of small aggregates with each other, leading to large agglomerates structured hierarchically. Furthermore, image analysis shows that the morphology of the aggregates, is also sensitive to temperature. The 3D distribution (size and circularity) and the fractal dimension D_2 also highlight that the aggregates formed after heating are larger and more circular. The ability to form consolidated aggregate during the heating step seems to be related to the intrinsic characteristics of the material. Indeed, the DMA (Dynamic Mechanical Analysis) analysis showed that the glass transition temperature of the MBS shell (polymethyl methacrylate) is around 90-100°C. In this interval, the mechanical properties of the latex evolve towards a greater deformability. This is reflected by the influence of the variation in heating temperature on the size and shape distributions and on the fractal dimensions D_2 and D_3 . Consequently, the higher the temperature, the larger and more circular the aggregates. In other words, the closer the heating temperature is to the glass transition temperature, the more aggregation is favored. A clear dependence was shown between the temperature (during the heating step) and the fact that the agglomeration was favored. The closer the heating temperature is to the glass transition, the larger and circular agglomerates are formed. The glass transition temperature of PMMA (shell material of the MBS latex) is around 95-100°C. All experiments were carried out at lower temperatures (42, 60, 80 and 95 °C), so sintering, strictly speaking, does not occur, except possibly for the test carried out at 95°C. So, the major mechanism and observed effect of temperature are probably due to the fact that as the temperature approaches the glass transition temperature, the aggregates become stickier and more deformable, which favors agglomeration efficiency and the formation of more circular-shaped aggregates.

The impact of hydrodynamics on the morphological properties of the aggregate population obtained in a stirred pilot reactor is now under further investigation. This experimental database will then be used in a perspective of development generic tools allowing an advance understanding of the suspension aggregation processes in order to control the morphological properties of the solid product formed and to propose innovations on the design of the reactors.

Acknowledgments

The authors thank the Agence Nationale de la Recherche (ANR) in France which founded this research, project ANR-20-CE07-0025-01.

Glossary

A: surface (m^2)
 A_s : intrinsic surface (m^2)
c: consistency coefficient (-)
C: circularity (-)
 C_a : acid concentration (mol/L)
CED: circle equivalent diameter (m)
D: impeller diameter (m)
DMA: Dynamic Mechanical Analysis
 D_3 : global fractal dimension (-)
 D_2 : 2D-fractal dimension (-)

I: scattering intensity (s^{-1})
k: modulus of the scattering wave vector (m^{-1})
 l_c : characteristic length (m)
MBS: Methacrylate Butadiene Styrene
m: rate constant (-)
N: stirring speed ($rev.s^{-1}$)
 N_p : power number (-)
 P_w : power (W)
P: perimeter (m)
 $\tan \delta$: dissipation factor (-)
T: temperature (K)
 T_1 : temperature of destabilization step ($^{\circ}C$)
 T_2 : temperature of heating step ($^{\circ}C$)
V: volume (m^3)

ε : viscous dissipation of the kinetic energy ($m^2.s^{-3}$)
 $\dot{\gamma}$: shear rate (s^{-1})
 λ : wavelength (m)
 μ : apparent viscosity (Pa.s)
 ν : kinematic viscosity ($m^2.s^{-1}$)
 η : Kolmogorov microscale (m)
 θ : scattering angle (rad)
 ρ : density ($kg.m^{-3}$)

References

- [1] Li, Y.; Xu, G.; Chen, M.; Wang, K. Slow Pelleting Coagulation of MBS Latex. *Chemical Engineering Research and Design* **1997**, *75* (1), 81–86. <https://doi.org/10.1205/026387697523246>.
- [2] Zhou, C.; Liu, H.; Chen, M.; Wu, G.; Zhang, H. Toughening of Polyvinylchloride by Methyl Methacrylate–Butadiene–Styrene Core–Shell Rubber Particles: Influence of Rubber Particle Size. *Polymer Engineering & Science* **2012**, *52* (12), 2523–2529. <https://doi.org/10.1002/pen.23210>.
- [3] Chen, X. D.; Wang, J. S.; Shen, J. R. Effect of the Shell Thickness of Methacrylate–Butadiene–Styrene Core–Shell Impact Modifier on Toughening Polyvinyl Chloride. *J Polym Res* **2006**, *13* (4), 335–341. <https://doi.org/10.1007/s10965-006-9048-8>.
- [4] Zhou, C.; Wu, S.; Liu, H.; Wu, G. Effects of Core-Shell Particle Growth Manners on Morphologies and Properties of Poly(Vinyl Chloride)/(Methyl Methacrylate–Butadiene–Styrene) Blends. *Journal of Vinyl and Additive Technology* **2016**, *22* (1), 37–42. <https://doi.org/10.1002/vnl.21438>.
- [5] Duan, J.; Gregory, J. Coagulation by Hydrolysing Metal Salts. *Advances in Colloid and Interface Science* **2003**, *100–102*, 475–502. [https://doi.org/10.1016/S0001-8686\(02\)00067-2](https://doi.org/10.1016/S0001-8686(02)00067-2).
- [6] Spicer, P. T.; Pratsinis, S. E. Shear-Induced Flocculation: The Evolution of Floc Structure and the Shape of the Size Distribution at Steady State. *Water Research* **1996**, *30* (5), 1049–1056. [https://doi.org/10.1016/0043-1354\(95\)00253-7](https://doi.org/10.1016/0043-1354(95)00253-7).
- [7] Kusters, K. A.; Wijers, J. G.; Thoenes, D. Aggregation Kinetics of Small Particles in Agitated Vessels. *Chemical Engineering Science* **1997**, *52* (1), 107–121. [https://doi.org/10.1016/S0009-2509\(96\)00375-2](https://doi.org/10.1016/S0009-2509(96)00375-2).
- [8] Selomulya, C.; Amal, R.; Bushell, G.; Waite, T. D. Evidence of Shear Rate Dependence on Restructuring and Breakup of Latex Aggregates. *Journal of Colloid and Interface Science* **2001**, *236* (1), 67–77. <https://doi.org/10.1006/jcis.2000.7372>.
- [9] Vaccaro, A.; Šefčík, J.; Wu, H.; Morbidelli, M.; Bobet, J.; Fringant, C. Aggregation of Concentrated Polymer Latex in Stirred Vessels. *AIChE Journal* **2006**, *52* (8), 2742–2756. <https://doi.org/10.1002/aic.10843>.
- [10] Soos, M.; Moussa, A. S.; Ehrl, L.; Sefcik, J.; Wu, H.; Morbidelli, M. Effect of Shear Rate on Aggregate Size and Morphology Investigated under Turbulent Conditions in Stirred Tank. *Journal of Colloid and Interface Science* **2008**, *319* (2), 577–589. <https://doi.org/10.1016/j.jcis.2007.12.005>.
- [11] Frappier, G.; Lartiges, B. S.; Skali-Lami, S. Floc Cohesive Force in Reversible Aggregation: A Couette Laminar Flow Investigation. *Langmuir* **2010**, *26* (13), 10475–10488. <https://doi.org/10.1021/la9046947>.
- [12] Guérin, L.; Coufort-Saudejaud, C.; Liné, A.; Frances, C. Dynamics of Aggregate Size and Shape Properties under Sequenced Flocculation in a Turbulent Taylor-Couette Reactor. *Journal of Colloid and Interface Science* **2017**, *491*, 167–178. <https://doi.org/10.1016/j.jcis.2016.12.042>.
- [13] Guérin, L.; Frances, C.; Liné, A.; Coufort-Saudejaud, C. Fractal Dimensions and Morphological Characteristics of Aggregates Formed in Different Physico-Chemical and Mechanical Flocculation Environments. *Colloids and Surfaces A: Physicochemical and Engineering Aspects* **2019**, *560*, 213–222. <https://doi.org/10.1016/j.colsurfa.2018.10.017>.
- [14] Ehrl, L.; Soos, M.; Morbidelli, M. Dependence of Aggregate Strength, Structure, and Light Scattering Properties on Primary Particle Size under Turbulent Conditions in Stirred Tank. *Langmuir* **2008**, *24* (7), 3070–3081. <https://doi.org/10.1021/la7032302>.

- [15] Kostansek, E. Controlled Coagulation of Emulsion Polymers. *Journal of Coatings Technology and Research* **2004**, *1*, 41–44. <https://doi.org/10.1007/s11998-004-0023-1>.
- [16] Navarro C., Girois S., Bay E., Saint-Martin J.-C. Process for Core-Shell Impact Modifiers and Impact Modified Thermoplastic Composition with Enhanced Hydrolytic Resistance. SG182095A1, July 30, 2012.
- [17] Gregory, J. Monitoring Particle Aggregation Processes. *Advances in Colloid and Interface Science* **2009**, *147–148*, 109–123. <https://doi.org/10.1016/j.cis.2008.09.003>.
- [18] Lachin, K.; Le Sauze, N.; Di Miceli Raimondi, N.; Aubin, J.; Gourdon, C.; Cabassud, M. Aggregation and Breakup of Acrylic Latex Particles inside Millimetric Scale Reactors. *Chemical Engineering and Processing: Process Intensification* **2017**, *113*, 65–73. <https://doi.org/10.1016/j.cep.2016.09.021>.
- [19] Soos, M., Ehrl, L., Bäbler, M.U., Morbidelli, M. Aggregate Breakup in a Contracting Nozzle. *Langmuir* **2010**, *26*, 10-18. <https://doi.org/10.1021/la903982n>.
- [20] Sorensen, C.M., Light Scattering by Fractal Aggregates: A Review. *Aerosol Sci. Technol.* **2001**, *35*, 648–687. <https://doi.org/10.1080/02786820117868>.
- [21] Vlieghe, M.; Frances, C.; Coufort- Saudejaud, C.; Liné, A. Morphological Properties of Floes under Turbulent Break- up and Restructuring Processes. *AICHE J.* **2017**, *63* (9), 3706–3716. <https://doi.org/10.1002/aic.15745>.
- [22] Florio, B. J.; Fawell, P. D.; Small, M. The Use of the Perimeter-Area Method to Calculate the Fractal Dimension of Aggregates. *Powder Technology* **2019**, *343*, 551–559. <https://doi.org/10.1016/j.powtec.2018.11.030>.
- [23] Sze, A.; Erickson, D.; Ren, L.; Li, D. Zeta-Potential Measurement Using the Smoluchowski Equation and the Slope of the Current–Time Relationship in Electroosmotic Flow. *Journal of Colloid and Interface Science* **2003**, *261* (2), 402–410. [https://doi.org/10.1016/S0021-9797\(03\)00142-5](https://doi.org/10.1016/S0021-9797(03)00142-5).
- [24] Hunter R.J., (1981), Zeta potential in colloid science, Academic Press. ISBN: 9781483214085
- [25] Saba, N.; Jawaid, M.; Alothman, O. Y.; Paridah, M. T. A Review on Dynamic Mechanical Properties of Natural Fibre Reinforced Polymer Composites. *Construction and Building Materials* **2016**, *106*, 149–159. <https://doi.org/10.1016/j.conbuildmat.2015.12.075>.
- [26] Sun, J.; Jiang, Y.; Zhou, X.; Ning, B.; Qin, H.; Kan, C. Agglomeration of the Poly(Butadiene-Styrene) Latex Triggered by CO₂ Bubbling and the Preparation of Poly(Methyl Methacrylate-Butadiene-Styrene) Core/Shell Particles with a Wide Size Distribution. *Micro & Nano Letters* **2018**, *13* (10), 1486–1490. <https://doi.org/10.1049/mnl.2018.5305>.
- [27] Takayasu, M. M.; Galembeck, F. Determination of the Equivalent Radii and Fractal Dimension of Polystyrene Latex Aggregates from Sedimentation Coefficients. *Journal of Colloid and Interface Science* **1998**, *202* (1), 84–88. <https://doi.org/10.1006/jcis.1998.5428>.
- [28] Vlieghe, M.; Coufort-Saudejaud, C.; Liné, A.; Frances, C. QMOM-Based Population Balance Model Involving a Fractal Dimension for the Flocculation of Latex Particles. *Chemical Engineering Science* **2016**, *155*, 65–82. <https://doi.org/10.1016/j.ces.2016.07.044>.
- [29] Spicer, P. T.; Pratsinis, S. E.; Raper, J.; Amal, R.; Bushell, G.; Meesters, G. Effect of Shear Schedule on Particle Size, Density, and Structure during Flocculation in Stirred Tanks. *Powder Technology* **1998**, *97* (1), 26–34. [https://doi.org/10.1016/S0032-5910\(97\)03389-5](https://doi.org/10.1016/S0032-5910(97)03389-5).

- [30] Oles, V. Shear-Induced Aggregation and Breakup of Polystyrene Latex Particles. *Journal of Colloid and Interface Science* **1992**, 154 (2), 351–358. [https://doi.org/10.1016/0021-9797\(92\)90149-G](https://doi.org/10.1016/0021-9797(92)90149-G).
- [31] Bouyer, D.; Coufort, C.; Liné, A.; Do-Quang, Z. Experimental Analysis of Floc Size Distributions in a 1-L Jar under Different Hydrodynamics and Physicochemical Conditions. *Journal of Colloid and Interface Science* **2005**, 292 (2), 413–428. <https://doi.org/10.1016/j.jcis.2005.06.011>.
- [32] Li, T.; Zhu, Z.; Wang, D.; Yao, C.; Tang, H. The Strength and Fractal Dimension Characteristics of Alum–Kaolin Floccs. *International Journal of Mineral Processing* **2007**, 82 (1), 23–29. <https://doi.org/10.1016/j.minpro.2006.09.012>.
- [33] Xiao, F.; Lam, K. M.; Li, X. Y.; Zhong, R. S.; Zhang, X. H. PIV Characterisation of Flocculation Dynamics and Floc Structure in Water Treatment. *Colloids and Surfaces A: Physicochemical and Engineering Aspects* **2011**, 379 (1), 27–35. <https://doi.org/10.1016/j.colsurfa.2010.11.053>.
- [34] Wang, D.; Wu, R.; Jiang, Y.; Chow, C. W. K. Characterization of Floc Structure and Strength: Role of Changing Shear Rates under Various Coagulation Mechanisms. *Colloids and Surfaces A: Physicochemical and Engineering Aspects* **2011**, 379 (1), 36–42. <https://doi.org/10.1016/j.colsurfa.2010.11.048>.
- [35] Coufort, C.; Bouyer, D.; Liné, A. Flocculation Related to Local Hydrodynamics in a Taylor–Couette Reactor and in a Jar. *Chemical Engineering Science* **2005**, 60 (8), 2179–2192. <https://doi.org/10.1016/j.ces.2004.10.038>.
- [36] Coufort, C.; Dumas, C.; Bouyer, D.; Liné, A. Analysis of Floc Size Distributions in a Mixing Tank. *Chemical Engineering and Processing: Process Intensification* **2008**, 47 (3), 287–294. <https://doi.org/10.1016/j.cep.2007.01.009>.
- [37] Lee C., Kramer T. A. Prediction of three-dimensional fractal dimensions using the two-dimensional properties of fractal aggregates. *Advances in Colloid and Interface Science* **2004**, 112, 49-57. <https://doi.org/10.1016/j.cis.2004.07.001>.
- [38] Wang R., Singh A.K., Kolan S. R., Tsotsas E. Investigation of the relationship between the 2D and 3D box-counting fractal properties and power law fractal properties of aggregates, *Fractal Fract.* **2022**, 6, 728. <https://doi.org/10.3390/fractalfract6120728>.
- [39] Palzer S. The effect of glass transition on the desired and undesired agglomeration of amorphous food powders. *Chem. Eng. Sci.* **2005**, 60 (14), 39-59-3968. <https://doi.org/10.1016/j.ces.2005.02.015>.
- [40] Avilés-Avilés C., Dumoulin E.D., Turchiuli C. Fluidised bed agglomeration of particles with different glass transition temperatures. *Powder Technol.* **2015**, 270, 445-452. <https://doi.org/10.1016/j.powted.2014.03.026>
- [41] Rieck C., Schmidt M., Bück A., Tsotsas E. Monte Carlo modeling of binder-less spray agglomeration in fluidized beds, *AIChE J.* **2018**, 64 (10) 3582-3594. <https://doi.org/10.1002/aic.16349>
- [42] Qiao, R.; Deng, H.; Putz, K. W.; Brinson, L. C. Effect of Particle Agglomeration and Interphase on the Glass Transition Temperature of Polymer Nanocomposites. *Journal of Polymer Science Part B: Polymer Physics* **2011**, 49 (10), 740–748. <https://doi.org/10.1002/polb.22236>.
- [43] Zhang, X.; Loo, L. S. Study of Glass Transition and Reinforcement Mechanism in Polymer/Layered Silicate Nanocomposites. *Macromolecules* **2009**, 42 (14), 5196–5207. <https://doi.org/10.1021/ma9004154>.

List of Figures

- Figure 1: Volume, surface and number size distributions of the initial MBS nanoparticle suspension
- Figure 2: Zeta potential of MBS latex suspension versus pH
- Figure 3: Scheme of the experimental set-up for MBS aggregation experiments
- Figure 4: Experimental protocol
- Figure 5: Number, surface and volume size distributions of the initial suspension I (dotted lines), at the end of the destabilization step D (dashed lines), and at the end of the heating step H (continuous lines) – Exp #1
- Figure 6: Fractal dimension D_3 and Temperature versus time – Exp #1
- Figure 7: 3D distribution of size and circularity – Exp # 1.
- (a) Number and (b) Volume distributions at the end of the destabilization step.
- (c) Number and (d) Volume distributions at the end of the heating step
- (e) Image of the aggregated suspension recovered at the end of the destabilization step
- (f) Image of the aggregated suspension recovered at the end of the heating step
- Figure 8: Number and volume size distributions during the destabilization step for different acid concentrations (Exp #1, Exp #2, Exp #3). (a) $t=2\text{min}$, (b) $t=7\text{min}$, (c) $t=16\text{min}$.
- Figure 9: Number and volume distributions during the destabilization step for different T_1 (Exp #1, Exp #4 and Exp #5). (a) $t=2\text{min}$, (b) $t=7\text{min}$, (c) $t=16\text{min}$.
- Figure 10: Volume (a) and number (b) size distributions at the end of the heating step for different T_2
- Figure 11: D_2 and D_3 fractal dimensions versus Temperature (Exp. # 6 to Exp #9)
- Figure 12: DMA results - Tangent Delta versus Temperature ($^{\circ}\text{C}$) for 2 experiments with different heating temperatures: (a) $T_2=42^{\circ}\text{C}$ and (b) $T_2=95^{\circ}\text{C}$

Supplementary material

- Figure S1: Density of a 21.5%w suspension versus Temperature
- Figure S2: Rheological behavior of a 2.15%w suspension of nanoparticles
- Figure S3: Examples of some aggregates obtained at the end of the destabilization step and at the end of the heating step
- Figure S4: Determination of the global fractal dimension in the fractal regime from laser diffraction – Effect of the heating step temperature on the fractal dimension D_3 of aggregates

List of Tables

- Table 1: Experimental conditions for aggregation runs
- Table 2: Mode and median diameters of the initial suspension and at the end of the destabilization and heating steps
- Table 3: Mode and median diameters at the end of the heating step for different T_2

Supplementary materials

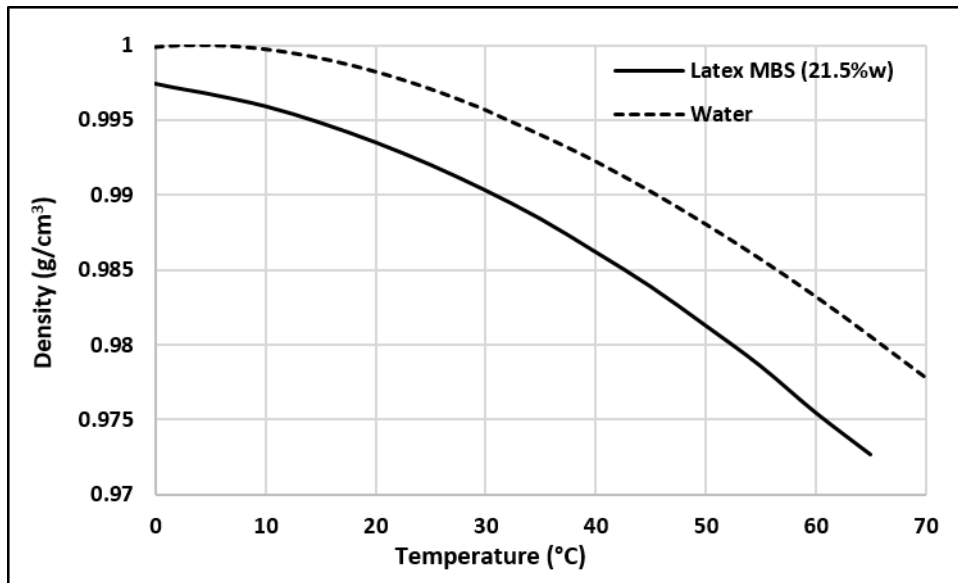


Figure S1: Density of a 21.5%w suspension versus Temperature

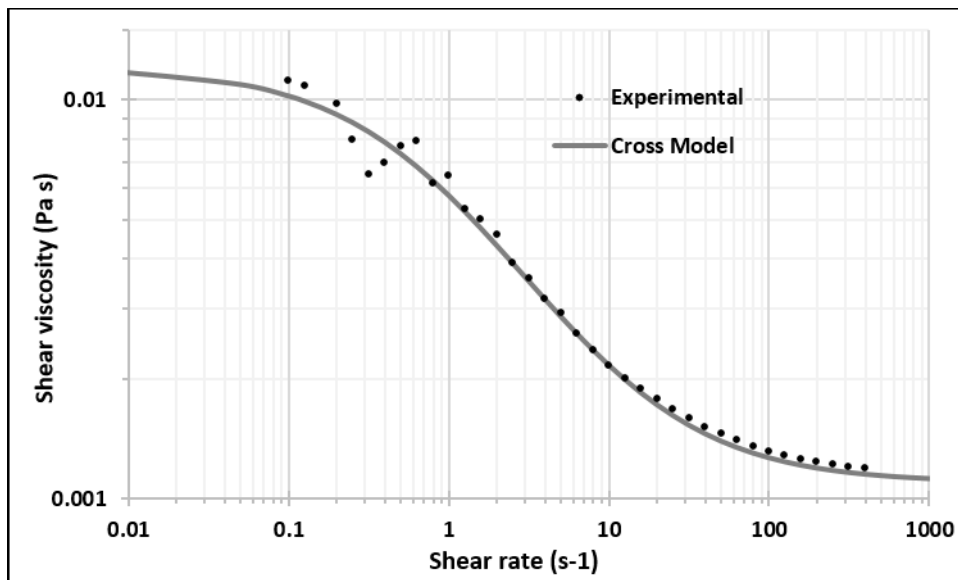
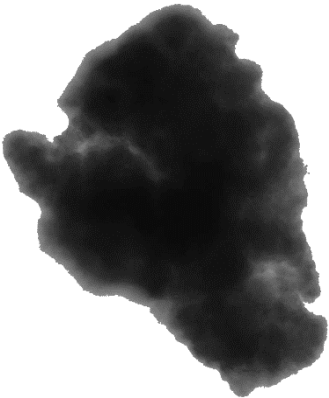
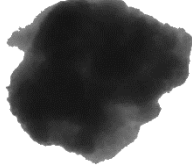


Figure S2: Rheological behavior of a 2.15%w suspension of nanoparticles

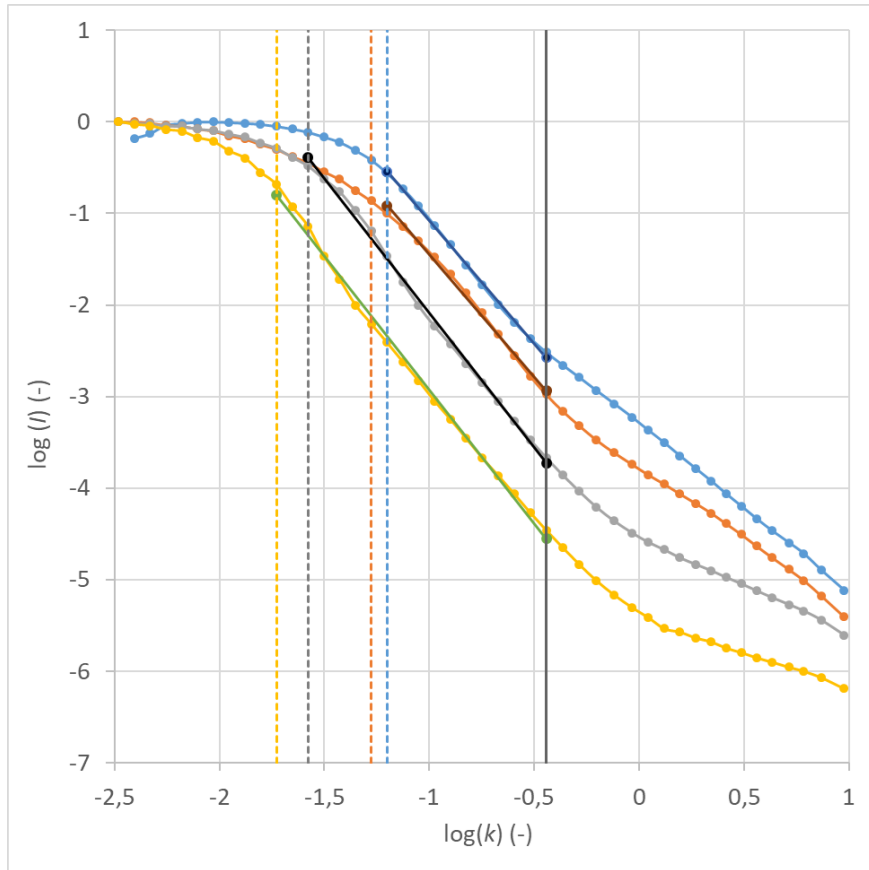
Destabilization step			Heating step		
Aggregate image	CED	C	Aggregate image	CED	C
	206.14	0.712		352.44	0.956
	170.82	0.797		297.78	0.954
	140.41	0.861		242.21	0.95

Destabilization step			Heating step		
Aggregate image	CED	C	Aggregate image	CED	C
	140.15	0.743		191.43	0.857
	110.19	0.673		168	0.957
	109.8	0.827		163.74	0.906
	80.24	0.644		92.94	0.969
	79.77	0.778		91.53	0.83
	40.2	0.884		60.92	0.75
	40.2	0.745		60.59	0.802
	13.8	0.839		32	0.813

CED : Circle Equivalent Diameter

C : Circularity

Figure S3: Examples of some aggregates obtained at the end of the destabilization step and at the end of the heating step



Heating Step Temperature	Symbol	Legend
42° C – Exp#6		Relative scattering intensity (I) versus the modulus of the scattering wave vector (k)
		$T_2=42^\circ\text{C}$: Lower limit estimate for the fractal regime
		$T_2=42^\circ\text{C}$: Fitting curve
60° C – Exp#7		Relative scattering intensity (I) versus the modulus of the scattering wave vector (k)
		$T_2=60^\circ\text{C}$: Lower limit estimate for the fractal regime
		$T_2=60^\circ\text{C}$ Fitting curve
80° C – Exp#8		Relative scattering intensity (I) versus the modulus of the scattering wave vector (k)
		$T_2=80^\circ\text{C}$: Lower limit estimate for the fractal regime
		$T_2=80^\circ\text{C}$: Fitting curve
95° C – Exp#9		Relative scattering intensity (I) versus the modulus of the scattering wave vector (k)
		$T_2=95^\circ\text{C}$: Lower limit estimate for the fractal regime
		$T_2=95^\circ\text{C}$: Fitting curve
		Upper limit estimate for the fractal regime

Figure S4: Determination of the global fractal dimension in the fractal regime from laser diffraction – Effect of the heating step temperature on the fractal dimension D_3 of aggregates